Research Square

Preprints are preliminary reports that have not undergone peer review.
They should not be considered conclusive, used to inform clinical practice,
or referenced by the media as validated information.

Diode Area Melting of Ti6Al4V: Effects of Multi-Laser Processing on Microstructure and Residual Stress

Anqi Liang

anqi45670@gmail.com

University of Sheffield

Sarath Veetil

University of Sheffield

Kristian Groom

University of Sheffield

Kamran Mumtaz

University of Sheffield

Research Article

Keywords: Diode area melting, Additive manufacturing, Residual stress, Ti6Al4V, Multiple diode lasers

Posted Date: June 25th, 2026

DOI: https://doi.org/10.21203/rs.3.rs-9968290/v1

License: This work is licensed under a Creative Commons Attribution 4.0 International License.
Read Full License

Additional Declarations: No competing interests reported.

Version of Record: A version of this preprint was published at Progress in Additive Manufacturing on September 8th, 2026. See the published version at https://doi.org/10.1007/s40964-026-01951-x.

Abstract

Laser Powder Bed Fusion (LPBF) is a widely adopted additive manufacturing technique for producing geometrically metal components. While this process yields fine microstructures beneficial for strength, the associated rapid thermal cycles generate steep temperature gradients and high residual stresses, which may lead to warping, cracking, and dimensional instability. Diode Area Melting (DAM) employs arrays of low-power diode lasers operating at shorter wavelengths (808 nm). The diode beams are integrated into a customised optical head that traverses the powder bed in the *X*-*Y* plane, enabling broader melt areas and reducing local cooling rate.

In this study, single-layer Ti6Al4V samples were processed using DAM with 3, 4, and 5 aligned diode lasers (wavelength of 808 nm and power of 5 W per laser). The effects of laser number and scanning speed (100, 150, 200, and 250 mm/min) on surface roughness, melt pool geometry, grain structure, cooling rate, and residual stress were systematically investigated. DAM produced significantly lower cooling rates (2211–8400 K/s) than those typically reported for LPBF (10^4–10^7 K/s), leading to coarser *α*-lath spacing (0.8–1.3 μm) and detectable *β*-phase formation. Residual tensile stresses in the DAM samples near the top surface were also reduced (up to 138.2 MPa). The simulated lower cooling rates and reduced residual stress indicate that DAM can provide an improved control over solidification behaviour and stress evolution in Ti6Al4V components.

1 Introduction

Laser powder bed fusion (LPBF) has recently attracted considerable interest in both industry and academia because of its advantages, including design flexibility, the ability to fabricate metal components with complex geometries, and its unique thermal history and features [1]. LPBF typically employs a galvo mirror system to rapidly reflect high-power fibre lasers or solid-state lasers (e.g. Nd:YAG), selectively melting thin layers of metal powders [2]. Diode area melting (DAM) is a novel alternative to LPBF that processes metals using multiple arrays of low-power diode laser emitters [3]. The main differences between DAM and LPBF are as follows: Firstly, DAM replaces the galvo system, which reflects a single fibre laser, with a gantry system that moves in *x*- / *y*- directions to maintain multiple laser beams in parallel. Secondly, DAM utilises diode lasers as a more efficient energy source due to their shorter wavelength compared to fibre lasers, which is particularly advantageous for highly reflective materials. For example, the absorptivity of Ti6Al4V powder melt with a single 808 nm diode laser increases by 14% compared with a 1064 nm fibre laser [4]. Thirdly, DAM employs multiple diode lasers arranged in a customised architectural array instead of a single fibre laser, enabling larger areas to be melted simultaneously. The layer-by-layer 2D geometry can be tailored by selectively activating lasers at specific locations [3], enabling more design flexibility than LPBF with a single fibre laser point.

Recent studies have demonstrated the feasibility of DAM for processing a range of metallic materials. Early work successful melted a full layer of Sn powder by using a hybrid energy source consisting of a diode laser array and a Q-switched pulsed laser [5]. Zavala-Arredondo et al. [6] processed 316L stainless

steel (SS) with 19 aligned 808 nm diode lasers (total beam area = 1.9 mm × 0.1 mm in a linear alignment of 1 × 19) and achieved a relative densities above 99% at an energy density of 86 J/mm^3. Their thermal simulations indicated that DAM can significantly reduce the temperature gradient (G) and cooling rates. Another study reported that the DAM-processed 316L SS exhibited a 100% increase in sub-grain cellular size compared with LPBF-fabricated 316L SS due to slower cooling rate [7]. The fabrication of 17-4PH stainless steel was also attempted using DAM with 19 diode lasers (total laser power of 50 W) [3]. However, with a layer thickness of 150 μm, the relative density was only 79.18% and lack-of-fusion porosity was observed due to inconsistencies in the manual deposition process.

Several studies have focused on DAM processing of Ti6Al4V alloys. Aydin et al. [8] reported that the low-power of 450 nm diode lasers produced slower solidification bahaviour and promoted the formation of a stable $\alpha + \beta$ phase with larger grain size. Caglar et al. [9] achieved near fully dense Ti6Al4V components (> 99% densification) using multiple 450 nm diode lasers and observed a coarser lamellar morphology than that typically reported for LPBF materials. Alsaddah et al. [4] compared 450 nm and 808 nm diode lasers for processing Ti6Al4V and they found that the laser absorption with 450 nm lasers was 11% higher than that with 808 nm lasers. Their work also reported that DAM cooling rate (1000–1670 °C/s) were significantly lower than those commonly reported for LPBF (~ 10^7 K/s), enabling the formation of β phases. However, the study about the effect of multi-laser interactions on the thermal penetration and residual stress development during DAM process are still limited.

Residual stress remains one of the main challenges in LPBF-built components due to rapid melting and solidification during repeated heating and cooling cycles [10]. Ahmed et al. [11] measured the residual stress in LPBF Ti6Al4V and found that tensile stress can exceed 900 MPa at the part edge, nearly reaching the yield strength. Machirori et al. [12] computed spatiotemporal variations of residual stress in LPBF Ti6Al4V, reporting tensile residual stresses of 800–920 MPa along the scanning direction and 500–760 MPa perpendicular to the scanning direction. Such stresses cause warpage and cracking and may promote failure when combined with service stresses, particularly under tensile condition [13]. Mercelis et al. [14] described residual stress formation in LPBF using the temperature gradient mechanism (TGM) and cool down models. During heating, irradiated material expands but is constrained by the surrounding material, leading to compressive stress. During cooling, the shrinkage is again constrained, creating residual tensile stresses. Although residual stress development in LPBF has been extensively investigated [15–17], corresponding studies on DAM-processed materials remain limited. Given the substantially lower cooling rates associated with DAM, residual stress development may differ significantly from that observed in LPBF.

Ti6Al4V is the most widely used titanium alloy because of its high specific strength, corrosion resistance, and biocompatibility. It is widely applied in aerospace [18], automotive [19], and biomechanical applications [20]. In this study, single-layer Ti6Al4V samples produced by DAM were investigated with particular emphasis on the relationship between laser configuration, thermal history, microstructure, and residual stress development. Previous studies on DAM Ti6Al4V have primarily focused on densification and process optimisation, whereas quantitative analysis of residual stress and

its correlation with local solidification behaviour remains limited. In addition to experimental characterisation, multi-laser thermal modelling was performed to estimate cooling rates under different laser configurations. The study aims to provide further insight into process–structure–stress relationships in DAM-processed Ti6Al4V.

2 Methodology

2.1 Experiment set up

DAM processing was conducted using a novel system developed at the University of Sheffield [21], as shown in Fig. 1. Figure 1(a) presents the schematic of the testing rig. The powder bed, powder feedstock and powder delivery system are identical to those in conventional LPBF systems. The novelty of DAM lies in the optical system, where 100 optical fibres are coupled into a custom-made laser head, enabling coupling allowing integration with up to 100 low-wavelength diode lasers as the laser source. The distribution of 100 fibres is shown as Fig. 1(b), they are arranged in a compact 2 × 50 linear arrays with a 127 μm distance in between. A group of optical lenses is assembled to collimate and focus the laser beams at a focal length of 63.5 μm. Low-power diode lasers (up to 5 W each) with a wavelength of 808 nm were used in this study. At the focal plane, each laser beam exhibited an individual Gaussian profile with a spot size of 65 μm, while the distance between adjacent beams was reduced to 76.2 μm due to a magnification factor of × 0.6 produced by the lens group, as shown in Fig. 1(c).

2.2 Specimen manufacturing procedure

Gas-atomised Ti6Al4V powders (particle size distributed between 15 μm to 45 μm) used in this study were supplied by Carpenter Additive under the trade name *PowderRange Ti64*. The chemical composition specified by the manufacturer is listed in Table 1.

Table 1
Chemical composition (*wt*%) of Ti6Al4V alloy powders [22].

Ti	Al	V	Fe	O	C	N	H	Y
Bal.	5.5–6.5	3.5–4.5	0.25	0.13	0.08	0.03	0.0125	0.005

Prior to processing, the chamber of the DAM system was purged with argon gas to remove oxygen and prevent oxidation. Once the oxygen concentration in the chamber fell below 0.1%, the purge rate was reduced to maintain a stable low oxygen environment during scanning. The multi-laser head was controlled by Lightburn software to traverse above the powder bed in the *x*- / *y*- directions. The powder bed layer thickness was set to 1 mm to ensure sufficient heat penetration from the lasers while avoiding bonding between the specimen and the substrate, which can significantly affect residual stress distribution. Afte the DAM process, the melt pool did not reach the substrate so that it was separated easily. The processing parameters are summarized in Table 2. Four scanning speeds (the traverse speed of the multi-laser head)—100, 150, 200, and 250 mm/min—were applied using three, four, and five

activated lasers (total laser powers of 15 W, 20 W, and 25 W, separately). A constant hatch spacing (*h*) of 200 μm (distance between two adjacent tracks) was applied for all specimens. The melt pool width varied with the number of activated lasers: 217 μm for three lasers, 294 μm for four lasers and 370 μm for five lasers. The scanning strategy is illustrated schematically in Fig. 2. The overlap extent (%) was calculated following the equation: (beam width – hatch spacing) ÷ beam width, and the results are also displayed below each schematic in Fig. 2. For each parameter set, three 10 mm × 10 mm single-layer samples were fabricated.

Table 2
Parameters for processing Ti6Al4V alloy.

	Total Laser power, *P* (W)	Scanning speed, *v* (mm/min)	Hatch spacing, *h* (μm)
3 lasers	15	100	200
		150	
		200	
		250	
4 lasers	20	100	200
		150	
		200	
		250	
5 lasers	25	100	200
		150	
		200	
		250	

2.3 Microstructure analysis

Surface roughness was measured using Alicona InfiniteFocusSL, which is a 3D profilometer employs variable focus measurement, and the colour contrast represents the relative height of each pixel. To minimize directional effects associated with the diode scanning paths, surface roughness measurements were performed using circular scan paths, providing a surface roughness (*Ra*) value independent of measurement direction. An average value was calculated from five measurements extracted from the top surfaces.

To prepare cross-sectional surfaces for microstructural characterization, specimens were first cut using a Buehler Isomet 5000 precision cutting machine equipped with a rotating blade operating at 2300 rpm and a feed rate of 0.15 mm/s. The sections were then mounted in PolyFast Resin, a conductive

thermosetting phenolic compound, using a Buehler Simplimet 1000 machine. Mounting was performed at 180 ℃ for 4 mins, followed by 2 mins of cooling. To achieve a mirror-like surface finish, the mounted samples were sequentially ground with #240, #600, #1200, #2500 and #4000 abrasive papers and then polished using 1 μm diamond paste.

Melt pools were observed using a Nikon LV150NL Upright Materials Microscope. Microstructure was examined with a TESCAN VEGA3 scanning electron microscope (SEM). Melt pool dimensions and heat affected zone dimensions were measured by Image J software, and five measurements were carried out for each image at random locations to calculate the average. Electron backscattered diffraction (EBSD) was used to investigate grain size, phase, and crystallographic orientation, using an Oxford Instruments® C-NANO EBSD detector operated at 20 kV. The step size was adjusted according to the scanning area to balance the resolution and acquisition time, with 0.1 μm at 650 × magnification. For EBSD specimens, final polishing was performed using a suspension of 90 vol% colloidal silica and 10 *vol*% hydrogen peroxide. EBSD data were analysed with AztecCrystal (Oxford Instruments) software, followed by a CI threshold of 0.1 and a nearest-neighbour cleanup procedure. Isolated incorrectly indexed pixels and unindexed pixels were replaced and filled with at least four indexed pixels surrounding them by using level 5 of Zero Solution Removal function. A misorientation angle of 15° was used to define grain boundaries. Grain morphology and size were assessed by calculating grain aspect ratios and average grain size. X-Ray Diffraction (XRD) was used to determine the phase using a PANalytical X'Pert^3 Powder diffractometer (Malvern Panalytical) with Cu Kα radiation (λ = 1.5406 Å). Data were recorded in the 2θ range of 10°–80° with a step size of 0.02° and a counting time of 2 s per step. The International Centre for Diffraction Data (ICDD) Powder Diffraction File (PDF) cards were used to match the structure of the material with the database. Measurements were performed in the reflective mode at 45 kV and 40 mA. Default divergence and anti-scatter slits were employed to optimise analytical conditions.

2.3 Residual stress analysis

Residual stress measurements were performed using X-ray diffraction (XRD) with a PANalytical X'Pert^3 Powder diffractometer, following the $\sin^2\psi$ method [23]. Due to the sample thickness, destructive methods such as hole drilling and contour cutting were not suitable for this study. XRD is a widely used non-destructive technique that enables residual stress evaluation without damaging the material, and it is recognized as an effective method for assessing residual stress in LPBF components [24, 25]. Residual stress of materials leads to a strain present within the crystal lattice, and the strain can be measured by XRD technique.

A Cu-Kα radiation source (45 kV, 40 mA) was employed, together with a beta-nickel filter to capture the diffracted X-rays. For Ti6Al4V, the (213) lattice plane, corresponding to a 2θ angle of 141.7° is commonly recommended for diffraction analysis, as it aligns with established standards and optimises measurement accuracy within the constraints of available X-ray wavelengths and instrumental capabilities [26]. Accordingly, the diffractometer was programmed to scan from 138.5510° to 143.4486°,

enabling precise determination of high-angle α-Ti peak positions at each tile angle. Then, the associated residual stress was calculated based on the principle that the distortion of the crystal lattice follows a linear elastic relationship, and a diffraction elastic modulus E_{213} = 110 GPa and Poisson's ratio v_{213} = 0.33 were used for stress evaluation [27]. For each sample, residual stress components were measured on the top surface in both directions that along the scanning direction (σ_{xx}) and perpendicular to scanning direction (σ_{yy}). The linear relationship between lattice spacing (d) and $\sin^2\psi$ was computed, and the slopes (M) of the linear fits in both orientations were determined [28]. X-ray penetration depth was relatively shallow, approximately 10 μm, so in this study only the near-surface stress was investigated.

2.4 Cooling rate simulation

The cooling rates of DAM Ti6Al4V specimens processed with 3, 4, and 5 lasers at scanning speeds ranging from 100 to 250 mm/min were simulated using the commercial computational fluid dynamic (CFD) software FLOW-3D™ (Flow Sciences, Inc.). This software employs the TruVOF (Volume of Fluid) method to track free surfaces and is built upon algorithms originally developed at Los Alamos National Laboratory. Temperature-time data were collected at the top centre of the laser beam. A further methodological details is available in a previous publication [29].

3 Results and discussion

3.1 Top morphology and surface roughness analysis

Surface roughness is an important characteristic of additive manufactured components because the irregular surface can act as a local stress concentrator, increasing localized tensile residual stresses. This makes the components more susceptible to cracking and can have a negative effect on the service lifetime of the components under cyclic loading. The top surface morphology and roughness of all the DAM specimens are shown in Fig. 3.

The measured *Ra* values varied considerably with laser configuration. Samples produced with 5 lasers appeared the smoothest surfaces (*Ra* = 1.2–1.3 μm), followed by the 4-laser condition, while the 3-laser group showed the roughest surfaces (*Ra* = 5.4–6.6 μm). This behaviour can be attributed to the overlap between adjacent melt tracks. As shown in Fig. 2, the melt pool width and the effective scanning area increase with the number of activated lasers. Under a constant hatch spacing, more activated lasers led to a greater overlap ratio between neighbouring tracks. In the 5-laser condition, approximately 45.9% of the melt pool with the subsequent scan, compared with only 7.8% in the 3-laser condition. The larger overlap ratio promoted partial remelting between adjacent tracks and reduced thermal discontinuities across the scanned region. As a result, melt pool stability improved and balling behaviour was suppressed. More uniform thermal conditions may also enhance Marangoni-driven melt flow, allowing redistribution of molten material before solidification and reducing height variations between neighbouring tracks. These effects contributed to the lower surface roughness observed in the five-laser samples.

Figure 3 also indicates a slight reduction in surface roughness with increasing scanning speeds. Under constant laser power and hatch spacing, higher scanning speeds reduce the energy density, lower recoil pressure and decrease heat penetration into the powder bed. Consequently, the melt pools become shallower, leading to a less curved molten pool surface, and thus lower surface roughness. Compared to the surface roughness (*Ra* in a range of 10–15 μm) reported for LPBF Ti6Al4V without post-processing [30], the DAM process produced a significant improvement of surface finish.

3.2 Melt pool observations

Representative cross-sectional images of the melt pools are shown in Fig. 4 for the sample processed using 5 lasers at a scanning speed of 100 mm/min. The OM image in Fig. 4(a) reveals several different regions: the melt pool, the heat affected zone (HAZ), and the surrounding Bakelite mounting material. Higher magnification SEM images in Fig. 4(b) shows that the HAZ consists of partially sintered powders bonded together, while the melt pool is fully melted and solidified. During the laser irradiation, the powder surface reaches temperatures above the melting point, resulting in complete melting and the formation of melt pools upon solidification. However, heat conducted into the powder bed is insufficient for completed melting. Consequently, loose powders beneath the melt pool undergo partial sintering rather than full consolidation, leading to the formation of the HAZ.

Figure 5 summarises the cross-sectional OM images of all the specimens produced using 3, 4, and 5 lasers at scanning speeds ranging from 100 to 250 mm/min. Clear differences in melt pool morphology were observed with varying laser configurations and scanning conditions. At a scanning speed of 100 mm/min, the 3-laser samples appeared relatively irregular melt pool shapes compared with the 4- and 5-laser samples.

This observation is consistent with higher surface roughness reported in the 3-laser samples, which was associated with the lower overlap ratio between adjacent tracks. Under constant hatch spacing, the limited overlap promoted less uniform remelting and increased local height variations between neighbouring tracks. This feature was most pronounced at lower scanning speeds, where higher energy input promoted more curved molten pools. As the scanning speed increased to 250 mm/min, the melt pools became less stable and more irregular. The higher scanning speed reduced the delivered energy density, limiting melt penetration and reducing the degree of melting within the powder bed [31]. The resulting melt pools were shallower and more susceptible to instability associated with insufficient fusion.

Figure 6 displays the variation in the melt pool depth and HAZ depth under different laser configurations and scanning conditions. Increasing the number of activated lasers generally increased both melt pool depth and HAZ depth, with the 5-laser samples absorbing the greatest heat penetration. At a scanning speed of 100 mm/min, the melt pool depth increased by nearly 17% from approximately 92 μm in the 3-laser samples to 108 μm in the 5-laser samples. A similar trend was observed for HAZ depth, which increased from 380 μm to 475 μm. The larger increase in HAZ depth compared with melt pool depth

indicates that the excessive thermal input significantly conducted to the subsurface than the melt penetration.

The total laser power increased from 15 W in the 3-laser configuration to 25 W in 5-laser configuration, while the corresponding scanning area is increased (217 μm for 3 lasers and 370 μm for 5 lasers). As a result, the energy density cannot be directly compared across different lasers configurations in DAM process. However, the deeper melt pools and HAZ regions observed in the 5-laser samples indicate greater overall thermal input and increased heat accumulation within the material.

For a given number of activated lasers, a lower scanning speed of 100 mm/min produced deeper melt pools and HAZ. In the 5-laser configuration, increasing scanning speed from 100 to 250 mm/min reduced the HAZ depth from approximately 475 μm to 345 μm, and the melt pool depth from around 108 μm to 95 μm. This indicates that scanning speed had a stronger influence on heat diffusion into the surrounding powder bed than on the fully molten region itself. The reduced thermal penetration at higher scanning speeds is attributed to the shorter laser–material interaction time and lower heat input per unit length.

3.3 Phase analysis

Ti6Al4V is a dual-phase titanium alloy consisting of a hexagonal close-packed (HCP) *α* phase, and a body-centred cubic (BCC) *β* phase [32]. XRD was used to identify the phases constitution of DAM Ti6Al4V specimens fabricated with 3, 4, and 5 lasers at scanning speeds between 100 and 250 mm/min. The corresponding 2*θ*-intensity plots are presented in Fig. 7. The dominant Bragg peaks correspond to *α*’ / *α*-Ti; however, the *α* and *α*’ phases cannot be reliably distinguished by conventional XRD due to their very similar lattice parameters. In addition to the *α*'/*α* matrix, a minor fraction of *β*-Ti peaks was detected at about 2*θ* = 39.5° in 4- and 5-laser specimens.

The presence of *β* phase in the DAM specimens is attributed to the reduced cooling rates associated with diode laser processing. In LPBF-fabricated Ti6Al4V, the extremely rapid cooling rates generally suppress diffusion-controlled phase transformations, promoting the formation of martensitic *α*' and limiting the retention of *β* phase [33]. In contrast, the lower cooling rates achieved in DAM provide a longer thermal exposure period, allowing vanadium partitioning and diffusion-controlled $\beta \rightarrow \alpha + \beta$ transformation during cooling [34]. As a result, measurable amounts of *β* phase can be retained in the as-built DAM specimens

The appearance of *β*-Ti peak was observed only in the 4- and 5-laser samples, but not in the 3-laser condition, suggests that a minimum thermal exposure may be necessary to enable sufficient vanadium partitioning and subsequent *β*-phase retention. The intensity of this peak was highest at the lowest scanning speed (100 mm/min) and gradually decreased with increasing scanning speed. The stronger *β*-phase intensity observed in the 4- and 5-laser specimens is consistent with the larger melt pools and deeper thermal penetration shown in Fig. 5 and Fig. 6. Increasing the number of activated lasers increased the overall thermal input and promoted heat accumulation within the melt pool region. The

resulting reduction in cooling rate favoured *β*-phase retention, whereas the higher scanning speeds reduced thermal exposure time and led to weaker *β*-phase diffraction peaks.

3.4 Grain structure

EBSD inverse pole figure (IPF) maps of all specimens are shown in Fig. 8(a), where different colours represent different crystallographic orientations. The microstructure is dominated by the Widmanstätten basket-weave morphology consisting of needle-shaped fine *α* / *α*' laths precipitated from the parent *β* phase. Clusters of similarly oriented *α* / *α*' laths are considered to have originated from an individual prior-*β* grain [35]. Coarse columnar prior-*β* grain boundaries are observed in several maps, an example is marked by a black dashed line in the 3-laser specimen processed at a scanning speed of 100 mm/min (top left corner). The contrast across these boundaries arises from orientation differences between α variants transformed from neighbouring prior-β grains during cooling.

The fine needle-shaped *α*-lath structure is observed in all maps, and the retained *β* phases are visible along prior- *β* grain boundaries or between *α* laths (pointed out by red arrows), particularly in specimens processed with 4- and 5-laser configurations at lower scanning speeds, which rarely exist in LPBF Ti6Al4V. This observation further supports the XRD phase analysis presented in Fig. 7, where detectable *β*-Ti peaks were observed only in samples subjected to greater thermal exposure. However, *β* regions were rarely identified in the 3-laser specimen processed at 250 mm/min because the faster cooling rate and limited thermal exposure suppress the $\beta \rightarrow \alpha + \beta$ transformation and favour a $\beta \rightarrow \alpha'$ transformation, producing fine and needle-like *α*' throughout the prior-*β* grains. Similar observations of retained *β* phase in DAM-processed Ti6Al4V have been reported previously [21].

Previous studies have shown that *α*-lath structure significantly affects mechanical behaviour of Ti6Al4V. Finer *α*-laths increase both dislocation density and boundary density. thereby effectively preventing the dislocation motion and contributing to higher yield strength and hardness [36, 37]. The measured *α*-lath spacings are displayed in Fig. 8(b). For all laser configurations, *α*-lath spacing decreased with increasing scanning speeds. In 5-laser specimens, *α*-lath spacing decreased from approximately 1.33 μm at 100 mm/min to 0.93 μm at 250 mm/min, corresponding to a reduction of about 30%. Similar reductions were observed in the 5-laser (26%) and 3-laser (27%) configurations.

The refinement of *α*-laths at higher scanning speeds is attributed to the increased cooling rate and solidification front velocity. Faster cooling promotes diffusional $\beta \rightarrow \alpha'$ transformation, increases undercooling, and limits the time available for lath growth, resulting in a finer α/α' microstructure. A clear effect of laser configuration was also observed. At a given scanning speed, the 5-laser specimens exhibited the coarsest α-laths, whereas the 3-laser specimens showed the finest microstructure. This trend closely follows the variation in melt pool and HAZ dimensions shown in Fig. 6. Samples exhibiting greater thermal penetration generally produced coarser α-laths, indicating slower cooling rates and longer thermal exposure during solidification.

Although the scanning area increased with the number of activated lasers, the higher total laser power and greater overlap ratio in 5-laser configuration results in localized heat accumulation, reduced solidification front velocity, and extended residence time above the *β*-transus, thereby promoting *α*-lath coarsening. Similar relationships between thermal conditions and *α*-lath spacing have been reported in other additive manufacturing processes. Scharowsky et al. [38] demonstrated that variations in energy input during electron beam melting (EBM) affect lamellar spacing due to variations in the solidification parameters, particularly the temperature gradient (*G*) and solidification front rate (*R*). Chen et al. [39] reported *α*-lath spacing of 0.7 ± 0.24 μm near the top surface of LPBF Ti6Al4V specimens. Another study reported average *α*-lath widths of 0.3 μm in as-built LPBF Ti6Al4V specimens [40]. The larger *α*-lath spacings measured in the present study are consistent with the substantially lower cooling rates associated with the DAM process.

3.5 Cooling rate simulation

The comparatively coarser *α* laths observed in DAM specimens are attributed to lower cooling rates relative to LPBF, which allow *α* lamellae to thicken through diffusional growth rather than forming a fully martensitic *α*′ microstructure. The simulated cooling rates for all processing conditions are presented in Fig. 9. The highest cooling rate of 8400 K/s was obtained at a scanning speed of 250 mm/min with 3 lasers, whereas the lowest cooling rate of 2211 K/s was recorded at 100 mm/min with 5 lasers. Although the cooling rates increased substantially with scanning speed and decreased with the number of activated lasers, all DAM conditions produced cooling rates considerably lower than those typically reported for LPBF Ti6Al4V, which can exceed 4×10^7 K/s [41]).

For a given laser configuration, increasing the scanning speed from 100 to 250 mm/min approximately doubled the cooling rate. This trend is attributed to the shorter laser–material interaction time and the higher solidification front velocity associated with faster scanning. In contrast, increasing the number of activated lasers reduced the cooling rate. The 5-laser configuration generated larger melt pools and deeper thermal penetration, as shown in Fig. 6, resulting in greater heat accumulation and a longer thermal lifetime of the molten region. Consequently, heat was dissipated more gradually, and solidification occurred over a longer period.

The cooling rate trends are consistent with the microstructural observations in Fig. 8. Conditions associated with lower cooling rates generally produced coarser *α*-laths and more pronounced *β*-phase retention, whereas higher cooling rates promoted finer *α*/*α*' lath structures. For example, the 5-laser specimen processed at 100 mm/min exhibited the lowest cooling rate (2211 K/s) and the largest *α*-lath spacing (1.33 μm), while the 3-laser specimen processed at 250 mm/min showed the highest cooling rate (8400 K/s) and the finest α-lath spacing (0.82 μm). These results indicate a clear relationship between thermal history and microstructural evolution in DAM-processed Ti6Al4V.

3.6 Residual stress

Residual stresses measured by XRD are presented in Fig. 10 (left), and the schematics of measurements directions σ_{xx} and σ_{yy} are illustrated in Fig. 10 (right). For all processing conditions, residual stresses

measured along the scanning direction (σ_{xx}) are consistently higher than those measured perpendicular to the scanning direction (σ_{yy}), with an average increase of approximately 53%. Similar anisotropic residual stress distributions have been reported for LPBF-fabricated Ti6Al4V [42, 43]. The higher stresses along the scanning direction are associated with the directional thermal history during the laser scanning. Continuous energy deposition promotes the elongated melt pools, while thermal contraction during cooling is constrained by neighbouring solidified material, generating tensile stresses along the scan path. In contrast, regions perpendicular to the scanning direction experience repeated thermal exposure from adjacent tracks, which can partially relax thermally induced stresses and reduce the magnitude of σ_{yy}.

A clear influence of laser configuration was observed. 3-laser specimens exhibited the highest residual stress (up to 138.2 MPa in the σ_{xx} direction and 91.3 MPa in the σ_{yy} direction). Residual stress decreased with increasing laser number, with the lowest values observed in the 5-laser specimens (up to 117.5 MPa in the σ_{xx} direction and 66.1 MPa in the σ_{yy} direction). Relative to the 3-laser specimens, the maximum σ_{yy} decreased by approximately 28%, whereas the maximum σ_{xx} decreased by about 15%. This trend is consistent with the larger melt pools, deeper thermal penetration, and lower cooling rates observed in the 4- and 5-laser configurations.

Scanning speed also influenced residual stress development. For all laser configurations, residual stress increased with scanning speed, with an overall increase of approximately 12.5–16.9% between 100 and 250 mm/min The higher cooling rates predicted at faster scanning speeds (Fig. 9) increase thermal contraction mismatch between the molten material and surrounding solidified regions, promoting elastic strain accumulation and higher tensile residual stresses. This behaviour is consistent with previous observations in LPBF Ti6Al4V, where increasing cooling rates are associated with higher tensile stress levels [44]. Although each sample was measured once by XRD based on the $\sin^2\psi$ method, the measured residual stress values showed a systematic trend with scanning speeds, the observed residual stress variations exhibit consistent and systematic trends across laser number and scanning speed, which correlate well with both the simulated cooling behaviour and the observed microstructural evolution. The agreement among these independent indicators provides converging evidence supporting the reliability of the observed stress trends, despite the limited statistical sampling.

The maximum tensile residual stress (138.2 MPa, at 250 mm/min with 3 lasers) remains significantly below the yield strength of LPBF Ti6Al4V (~ 1030 MPa [45]), indicating that there is no plastic deformation or warpage observed in the single-layer DAM specimens. It has been widely reported that LPBF Ti6Al4V specimens typically exhibit tensile residual stress near the top surface, with values up to 688.19 MPa [25, 46], higher than those obtained in this study. Compared with LPBF, lower cooling rates during DAM process promote a uniform thermal field and allows stress relaxation at high temperatures, thereby the high residual stresses commonly observed in LPBF parts can be effectively mitigated.

It should also be noted that the present work employed a single-layer configuration deposited onto a 1 mm powder bed. Under these conditions, residual stress development is dominated by intra-layer

thermal gradients and shrinkage constraints between neighbouring melt pools. The influence of substrate restraint and inter-layer stress accumulation, which are major contributors to residual stress in multi-layer LPBF builds, is therefore minimised. Consequently, the stress values reported here primarily reflect the intrinsic thermal response of the DAM process rather than stress accumulation associated with bulk component fabrication.

4 Conclusion

This study investigated the processing of Ti6Al4V alloys using an 808 nm multiple diode laser system and examined the influence of laser number and scanning speeds on surface roughness, melt pool dimensions, grain structure, cooling rate, and residual stress. The key summaries follow below:

- Single-layer Ti6Al4V components were successfully processed using multiple 808 nm wavelength diode lasers (3, 4, or 5 lasers aligned in an array), and dense surfaces without visible defects (lack-of-fusion defect or balling) were achieved.
- A smoother top surface with surface roughness (1.2–6.6 μm) was obtained in DAM Ti6Al4V than as-build LPBF Ti6Al4V components (10–15 μm) because the lower energy density and wide laser beam in DAM process made the melt pool less turbulent and provides a more stable and flatter surface. Such surface quality has the potential to suppress fatigue crack initiation and propagation, thereby extending service lifetime.
- DAM Ti6Al4V exhibited α-lath spacings in the range of 0.8–1.3 μm, which is coarser than those reported in LPBF Ti6Al4V due to the lower cooling rate. Slow cooling allows extended time for lath growth and reduces the nucleation density, resulting in thicker laths. Also, a small amount of β phases were detected in some DAM-processed specimens, while metastable acicular martensite phase (α') dominates the LPBF-processed Ti6Al4V.
- The tensile residual stress (up to 138.2 MPa) observed in DAM Ti6Al4V specimens at near top surface region is substantially lower than LPBF Ti6Al4V (around 688.19 MPa) due to the lower cooling rates (2211–8400 K/s). A low cooling rate can reduce the residual stress by providing sufficient time to release the stress during cooling though plastic deformation.

Overall, these results demonstrate that by employing multiple low-power diode lasers, the DAM process can effectively reduce residual stress while achieving high surface quality, offering promising potential for the reliable fabrication of multi-layer Ti6Al4V components. However, the present study is limited to single-layer DAM specimens. Future work will extend the investigation to multi-layer specimens to explore the effects of cumulative thermal cycling under more representative fabrication conditions.

Declarations

Author Contribution

All authors reviewed and contributed to the manuscript.

Acknowledgement

The authors gratefully acknowledge the support of the Engineering and Physical Sciences Research Council (EPSRC) through Grant [EP/W024764/1]. The author also thanks the Department of Mechanical Engineering at University of Sheffield for providing research facilities and technical support.

Data Availability

The data that support the findings of this study are available from the corresponding author upon reasonable request.

References

1. Cherry J, Davies H, Mehmood S, Lavery N, Brown S, Sienz J (2015) Investigation into the effect of process parameters on microstructural and physical properties of 316L stainless steel parts by selective laser melting. Int J Adv Manuf Technol 76:869–879
2. Pathania A, Subramaniyan AK, Nagesha B (2022) Influence of post-heat treatments on microstructural and mechanical properties of LPBF-processed Ti6Al4V alloy. Progress Additive Manuf 7(6):1323–1343
3. Zavala-Arredondo M, Boone N, Willmott J, Childs DT, Ivanov P, Groom KM, Mumtaz K (2017) Laser diode area melting for high speed additive manufacturing of metallic components. Mater Design 117:305–315
4. Alsaddah M, Khan A, Groom K, Mumtaz K (2021) Use of 450–808 nm diode lasers for efficient energy absorption during powder bed fusion of Ti6Al4V. Int J Adv Manuf Technol 113(9):2461–2480
5. Matthews MJ et al (2017) Diode-based additive manufacturing of metals using an optically-addressable light valve. Opt Express 25(10):11788–11800
6. Zavala-Arredondo M, Ali H, Groom KM, Mumtaz K (2018) Investigating the melt pool properties and thermal effects of multi-laser diode area melting. Int J Adv Manuf Technol 97(1):1383–1396
7. Erman SC, Aydin A, Groom K, Mumtaz K (2025) Diode area melting of SS316L using low power 450 nm lasers. Int J Adv Manuf Technol 136(10):4471–4490
8. Aydin A, Cetin E, Erman SC, Mumtaz K (2025) Laser powder bed fusion of Ti6Al4V using low-cost high efficiency 450 nm diode point melting. J Mater Res Technol 34:2814–2827
9. Caglar H, Liang A, Groom K, Mumtaz K (2024) Multi-laser powder bed fusion of Ti6Al4V: Diode area melting utilizing low-power 450 nm diode lasers. J Mater Process Technol 325. 10.1016/j.jmatprotec.2024.118303
10. Goel S, Neikter M, Capek J, Polatidis E, Colliander MH, Joshi S, Pederson R (2020) Residual stress determination by neutron diffraction in powder bed fusion-built Alloy 718: Influence of process parameters and post-treatment. Mater Design 195:109045

11. Ahmad B, van der Veen SO, Fitzpatrick ME, Guo H (2018) Residual stress evaluation in selective-laser-melting additively manufactured titanium (Ti-6Al-4V) and inconel 718 using the contour method and numerical simulation. Additive Manuf 22:571–582
12. Machirori T, Liu F, Yin Q, Wei H (2021) Spatiotemporal variations of residual stresses during multi-track and multi-layer deposition for laser powder bed fusion of Ti-6Al-4V. Comput Mater Sci 195:110462
13. Thijs L, Verhaeghe F, Craeghs T, Van Humbeeck J, Kruth J-P (2010) A study of the microstructural evolution during selective laser melting of Ti–6Al–4V. Acta Mater 58(9):3303–3312
14. Mercelis P, Kruth JP (2006) Residual stresses in selective laser sintering and selective laser melting. Rapid Prototyp J 12(5):254–265
15. Hosseini SM, Vaghefi E, Mirkoohi E (2023) The role of defect structure and residual stress on fatigue failure mechanisms of Ti-6Al-4V manufactured via laser powder bed fusion: Effect of process parameters and geometrical factors. J Manuf Process 102:549–563
16. Mishurova T et al (2021) Separation of the impact of residual stress and microstructure on the fatigue performance of LPBF Ti-6Al-4V at elevated temperature. Int J Fatigue 148:106239
17. Chen C, Chang S, Zhu J, Xiao Z, Zhu H, Zeng X (2020) Residual stress of typical parts in laser powder bed fusion. J Manuf Process 59:621–628
18. Manikandan P et al (2022) On the anisotropy in room-temperature mechanical properties of laser powder bed fusion processed Ti6Al4V-ELI alloy for aerospace applications. J Mater Sci 57(21):9599–9618
19. Shunmugavel M, Polishetty A, Littlefair G (2015) Microstructure and mechanical properties of wrought and additive manufactured Ti-6Al-4 V cylindrical bars. Procedia Technol 20:231–236
20. Cabrini M et al (2022) Influence of surface finishing and heat treatments on the corrosion resistance of LPBF-produced Ti-6Al-4V alloy for biomedical applications. J Mater Process Technol 308:117730
21. Alsaddah M, Khan A, Groom K, Mumtaz K (2022) Diode area melting of Ti6Al4V using 808 nm laser sources and variable multi-beam profiles. Mater Design 215:110518
22. Additive C Datasheet of PowderRange Ti64 https://www.carpenteradditive.com/powderrange-ti64 (accessed
23. X-RAY DIFFRACTION RESIDUAL PS (1986) STRESS TECHNIQUES in *Metals Handbook*, pp. 380–392
24. Serrano-Munoz I et al (2020) The residual stress in as-built Laser Powder Bed Fusion IN718 alloy as a consequence of the scanning strategy induced microstructure. Sci Rep 10(1):14645
25. Levkulich N, Semiatin S, Gockel J, Middendorf J, DeWald A, Klingbeil N (2019) The effect of process parameters on residual stress evolution and distortion in the laser powder bed fusion of Ti-6Al-4V. Additive Manuf 28:475–484
26. Noyan IC, Cohen JB (1987) Analysis of Residual Stress Fields Using Linear Elasticity Theory. *Residual Stress* (Materials Research and Engineering book series (MATERIALS). Springer, New York, NY, pp 47–74

27. Chen Q, Liu L, Zhu C, Chen K (2018) Mesomechanical modeling and numerical simulation of the diffraction elastic constants for Ti6Al4V polycrystalline alloy, *Metals*, vol. 8, no. 10, p. 822
28. Prevéy PS (1986) X-ray diffraction residual stress techniques. ASM Int ASM Handb 10:380–392
29. Alayil Veetil S (2024) Diode Area Melting of Ti6Al4V: Probing the Multi-laser Interaction and. Residual Stress Evolution, University of Sheffield
30. Lu D, Liu Z, Wei X, Chen C, Wang D (2023) Effect of post-processing methods on the surface quality of Ti6Al4V fabricated by laser powder bed fusion. Front Mater 10:1126749
31. Bhatt A et al (2023) In situ characterisation of surface roughness and its amplification during multilayer single-track laser powder bed fusion additive manufacturing. Additive Manuf 77:103809
32. Alpha + Beta (2007) Alloys. Titanium. Springer Berlin Heidelberg, Berlin, Heidelberg, pp 203–258
33. Cao S, Zou Y, Lim CVS, Wu X (2021) Review of laser powder bed fusion (LPBF) fabricated Ti-6Al-4V: process, post-process treatment, microstructure, and property. Light: Adv Manuf 2(3):313–332
34. Barriobero-Vila P et al (2017) Inducing stable α + β microstructures during selective laser melting of Ti-6Al-4V using intensified intrinsic heat treatments, *Materials*, vol. 10, no. 3, p. 268
35. Vrancken B, Thijs L, Kruth J-P, Van Humbeeck J (2012) Heat treatment of Ti6Al4V produced by Selective Laser Melting: Microstructure and mechanical properties. J Alloys Compd 541:177–185
36. Gil F, Ginebra M, Manero J, Planell J (2001) Formation of α-Widmanstätten structure: effects of grain size and cooling rate on the Widmanstätten morphologies and on the mechanical properties in Ti6Al4V alloy. J Alloys Compd 329(1–2):142–152
37. Galarraga H, Warren RJ, Lados DA, Dehoff RR, Kirka MM, Nandwana P (2017) Effects of heat treatments on microstructure and properties of Ti-6Al-4V ELI alloy fabricated by electron beam melting (EBM). Mater Sci Engineering: A 685:417–428
38. Scharowsky T, Juechter V, Singer RF, Körner C (2015) Influence of the scanning strategy on the microstructure and mechanical properties in selective electron beam melting of Ti–6Al–4V. Adv Eng Mater 17(11):1573–1578
39. Chen J, Fabijanic D, Brandt M, Zhao Y, Ren S, Xu W (2023) Dynamic α globularization in laser powder bed fusion additively manufactured Ti-6Al-4V. Acta Mater 255:119076
40. Yu G, Li Z, Hua Y, Liu H, Zhao X, Li W, Wang X (2020) The effects of post heat treatment on the microstructural and mechanical properties of an additive-manufactured porous titanium alloy, *Materials*, vol. 13, no. 3, p. 593
41. Hooper PA (2018) Melt pool temperature and cooling rates in laser powder bed fusion. Additive Manuf 22:548–559
42. Liu Y, Yang Y, Wang D (2016) A study on the residual stress during selective laser melting (SLM) of metallic powder. Int J Adv Manuf Technol 87:647–656
43. Robinson J, Ashton I, Fox P, Jones E, Sutcliffe C (2018) Determination of the effect of scan strategy on residual stress in laser powder bed fusion additive manufacturing. Additive Manuf 23:13–24

44. Ganeriwala R et al (2019) Evaluation of a thermomechanical model for prediction of residual stress during laser powder bed fusion of Ti-6Al-4V. Additive Manuf 27:489–502
45. Sun D et al (2019) Selective laser melting of titanium parts: Influence of laser process parameters on macro-and microstructures and tensile property. Powder Technol 342:371–379
46. Shaw PK, Dwivedi S, Dixit AR, Pramanik A (2025) Understanding residual stress and microhardness variations in laser powder bed fusion fabricated Ti-6Al-4V: Thermo-mechanical simulation and experimental insights post heat treatment. Int J Precision Eng Manufacturing-Green Technol 12(4):1309–1319

Figures

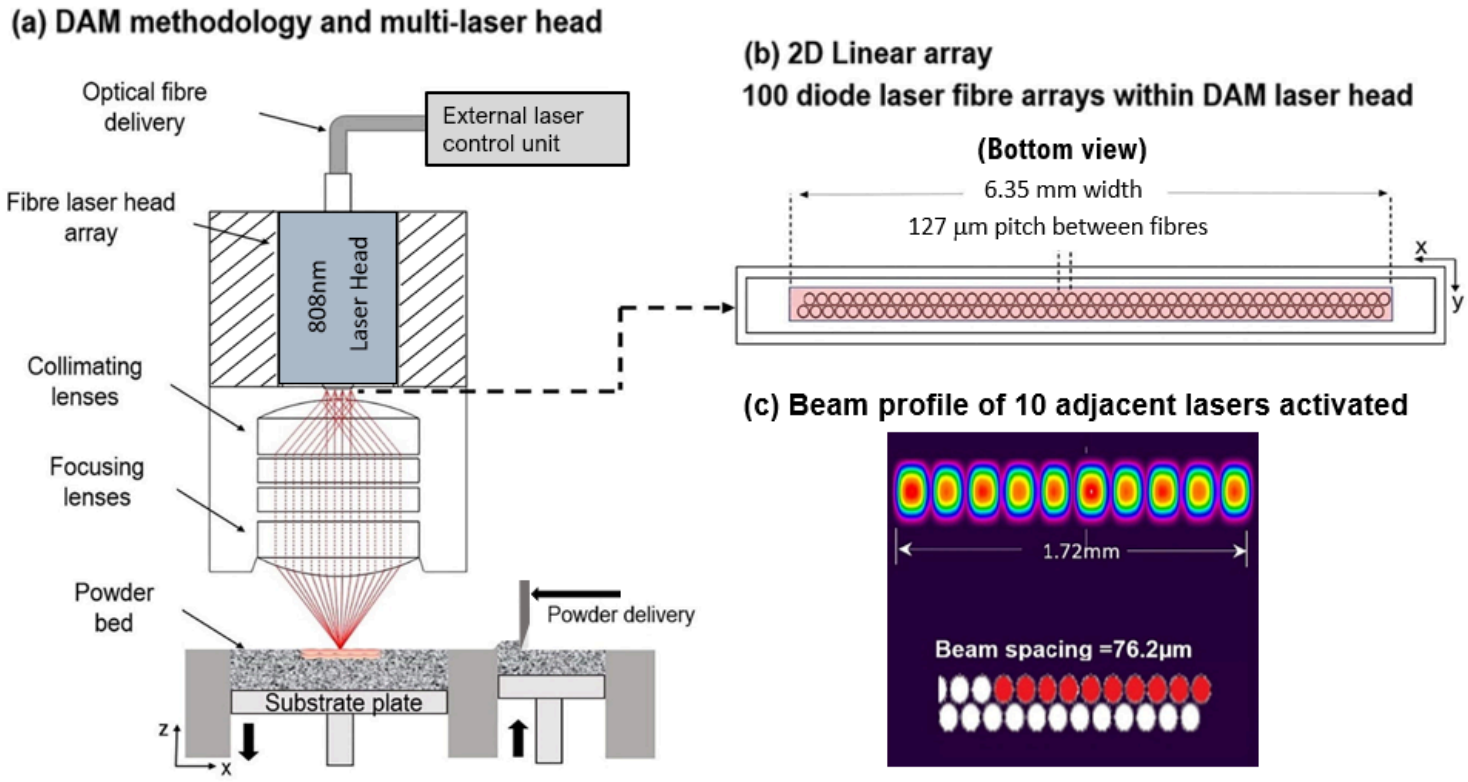


Figure 1

(a) Schematic of testing rig, (b) bottom view of the multiple laser beam configuration, and (c) beam profile of 10 adjacent lasers activated [21].

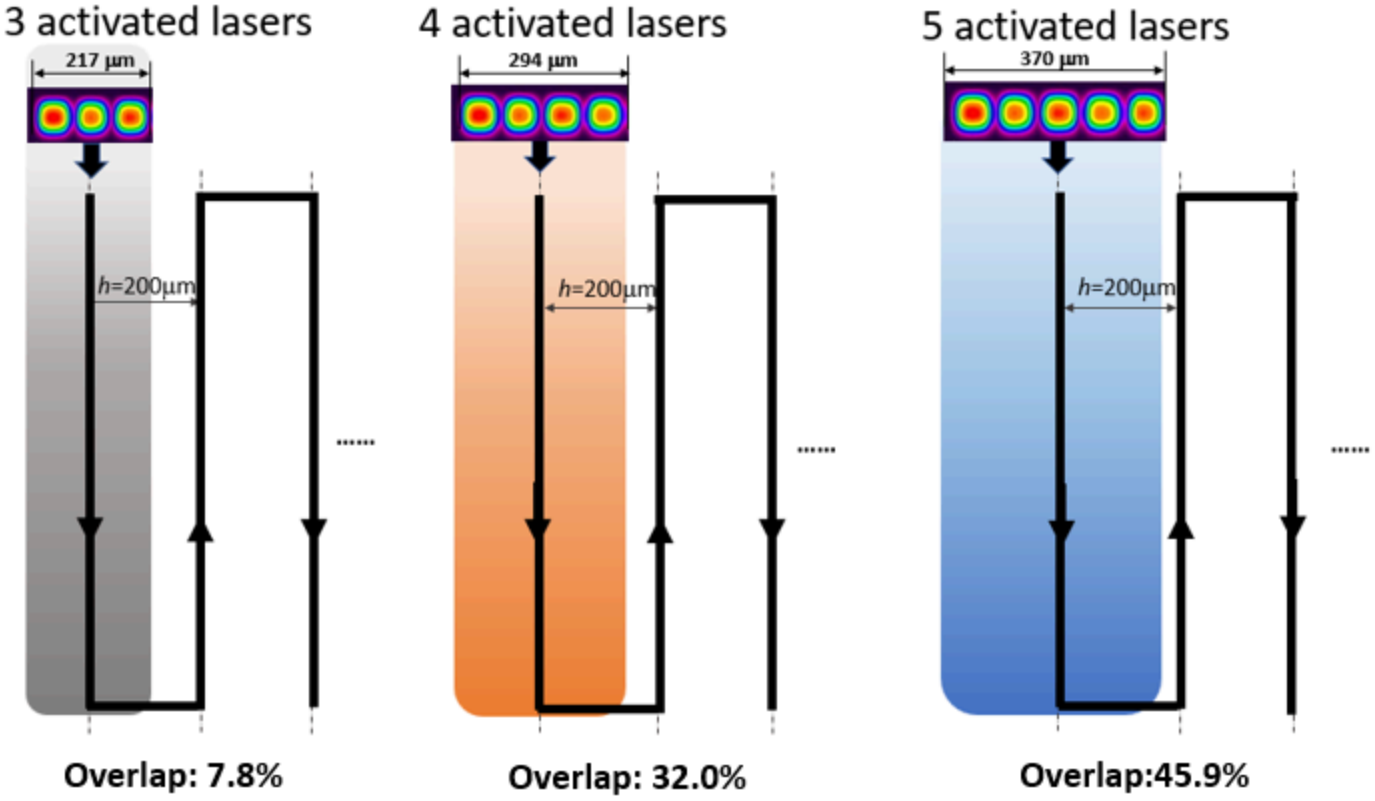


Figure 2

Schematic of scanning strategies with (a) 3 lasers, (b) 4 lasers, and (c) 5 lasers. The arrows represent the scanning direction of each path.

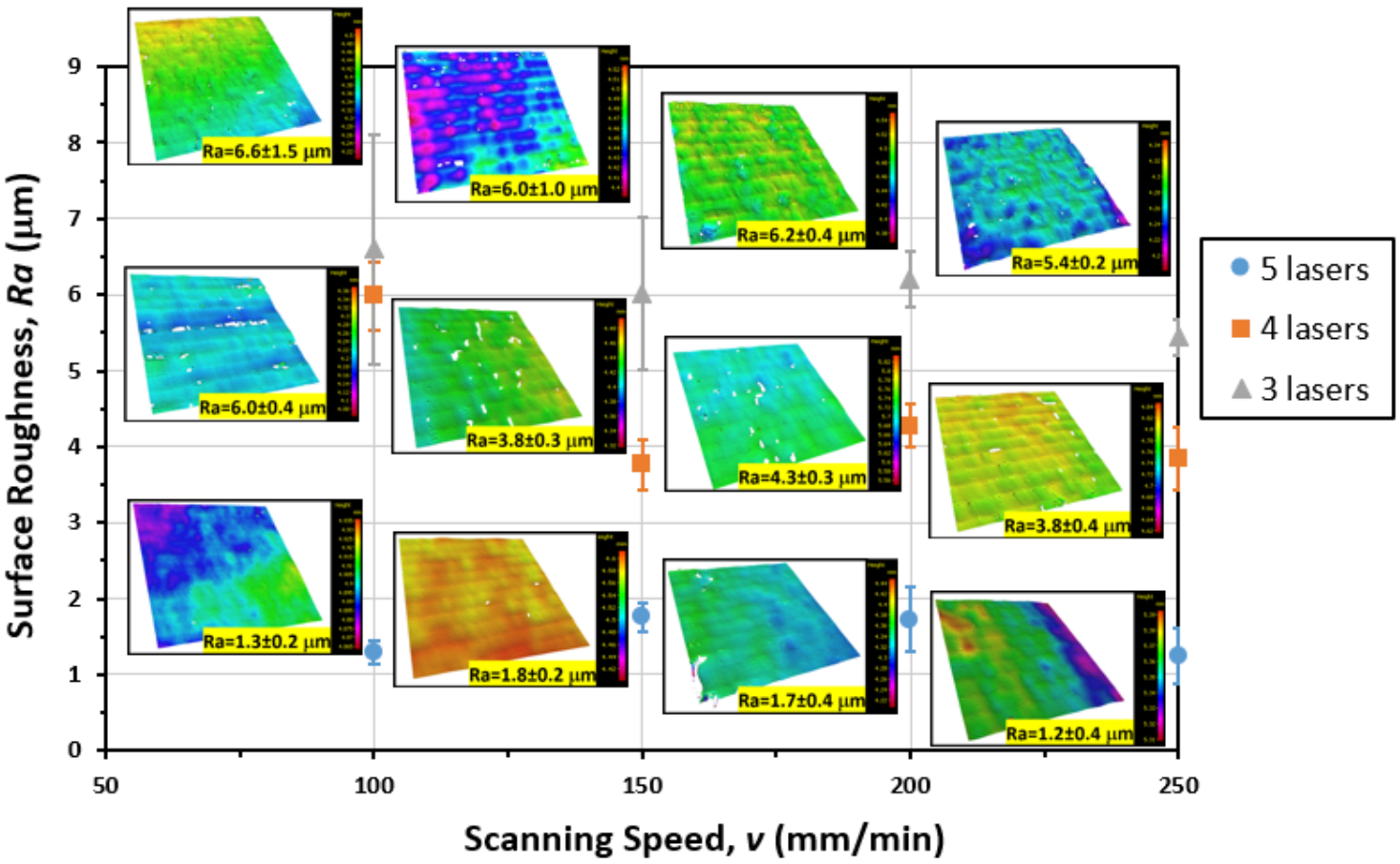


Figure 3

Top morphology and surface roughness (*Ra*) of specimens fabricated with 3 lasers (gray data), 4 lasers (orange data), and 5 lasers (blue data) using varying scanning speeds.

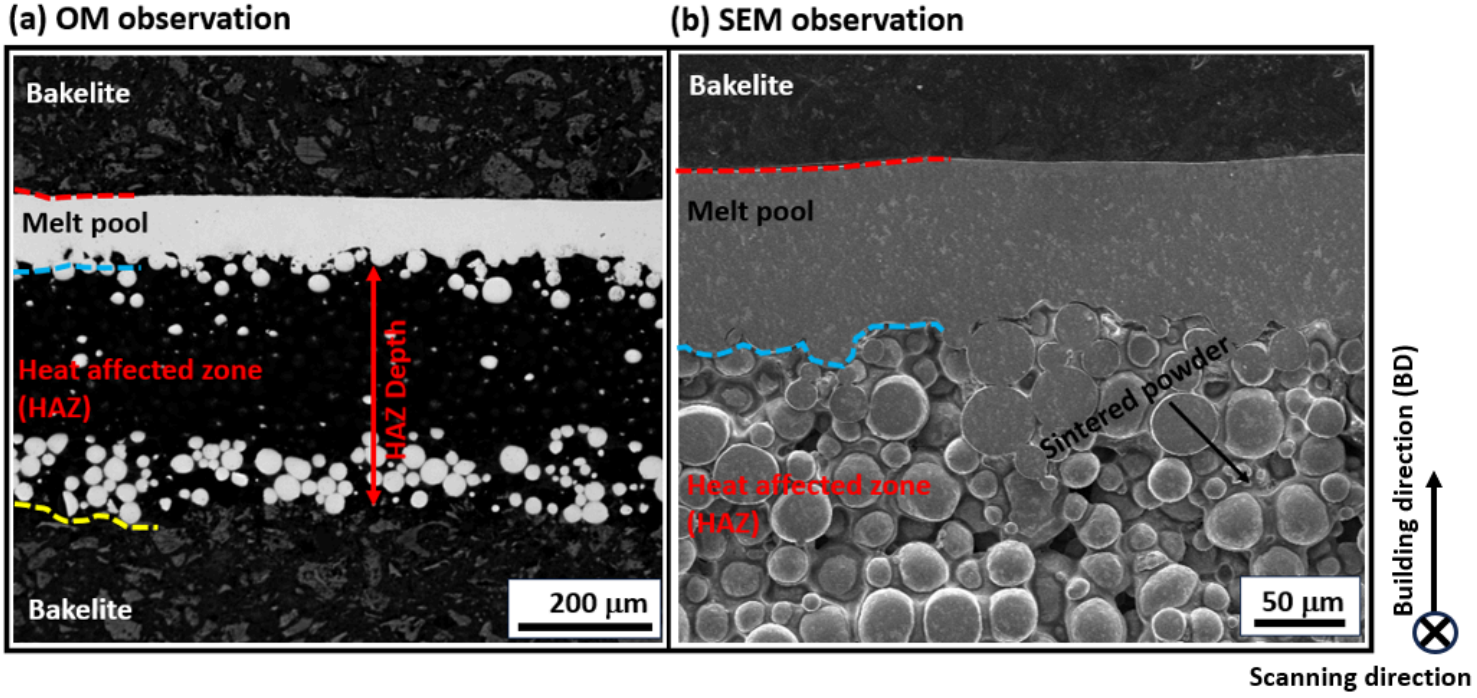


Figure 4

Cross-sectional (a) OM images and (b) SEM images of specimens fabricated with 5 lasers at a scanning speed of 100 mm/min.

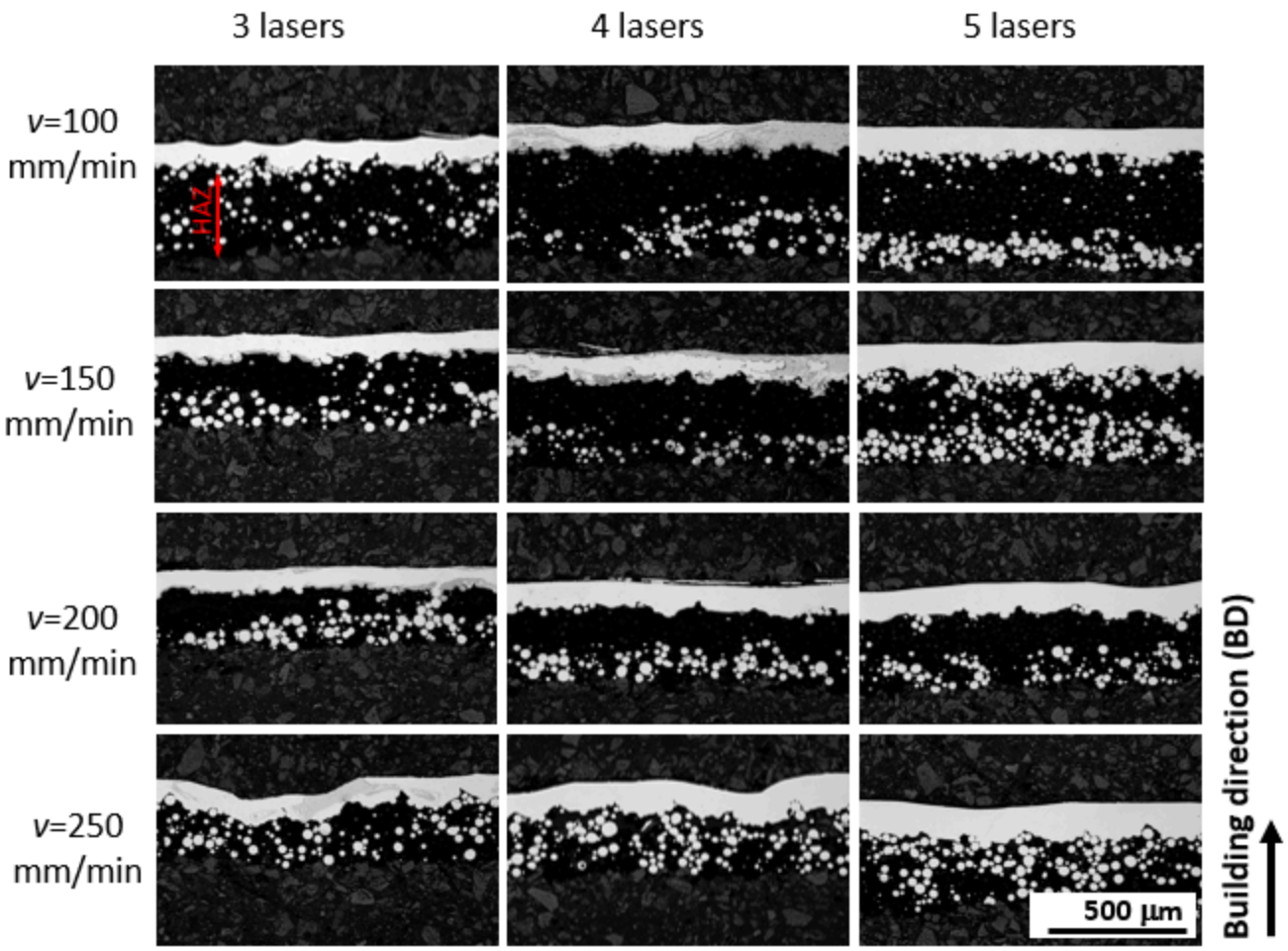


Figure 5

Cross-sectional OM images of specimens fabricated with 3, 4, and 5 lasers using varying scanning speeds.

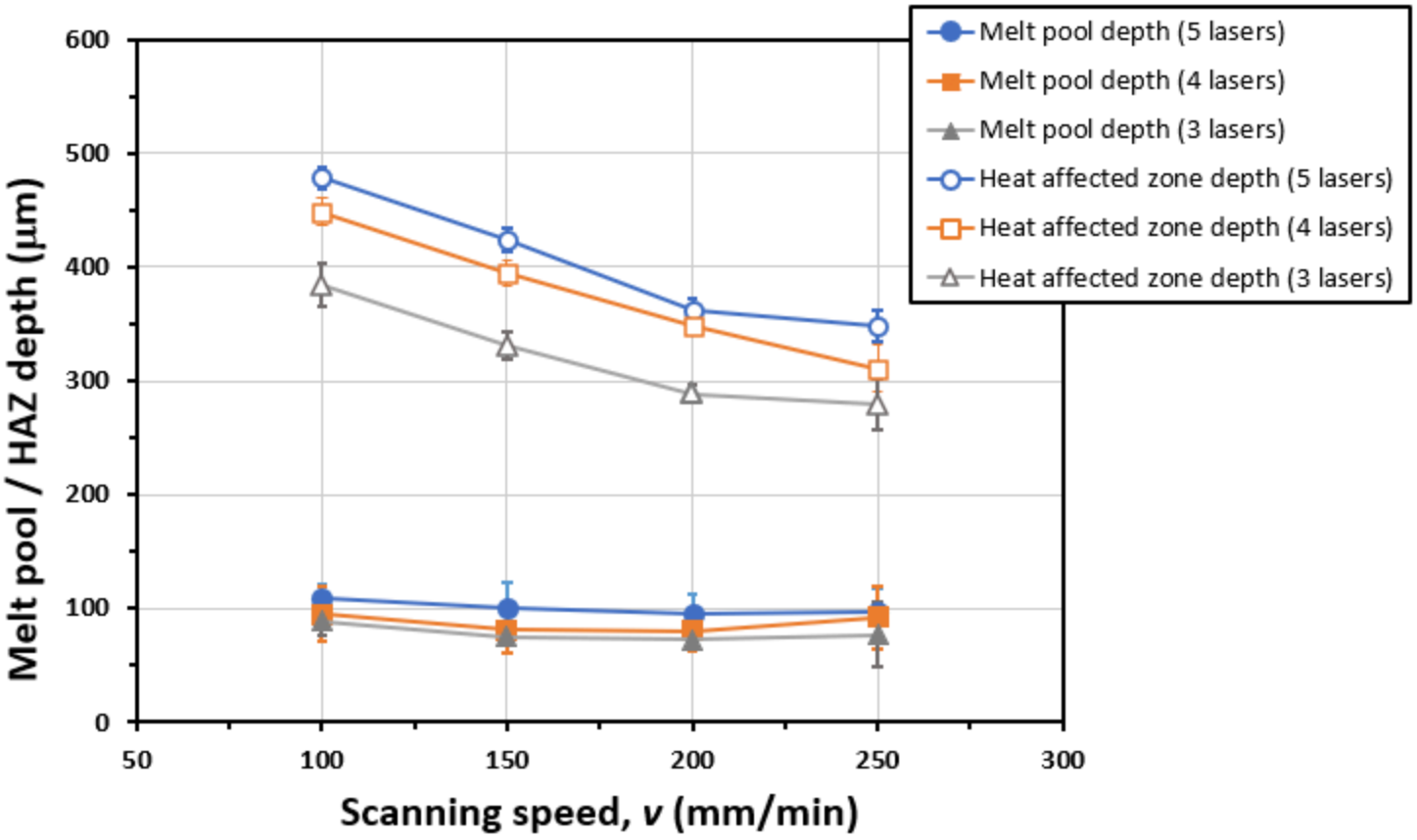


Figure 6

Plot of melt pool depth and heat affected zone vs. scanning speeds for specimens fabricated with 3 lasers (gray data), 4 lasers (orange data), and 5 lasers (blue data).

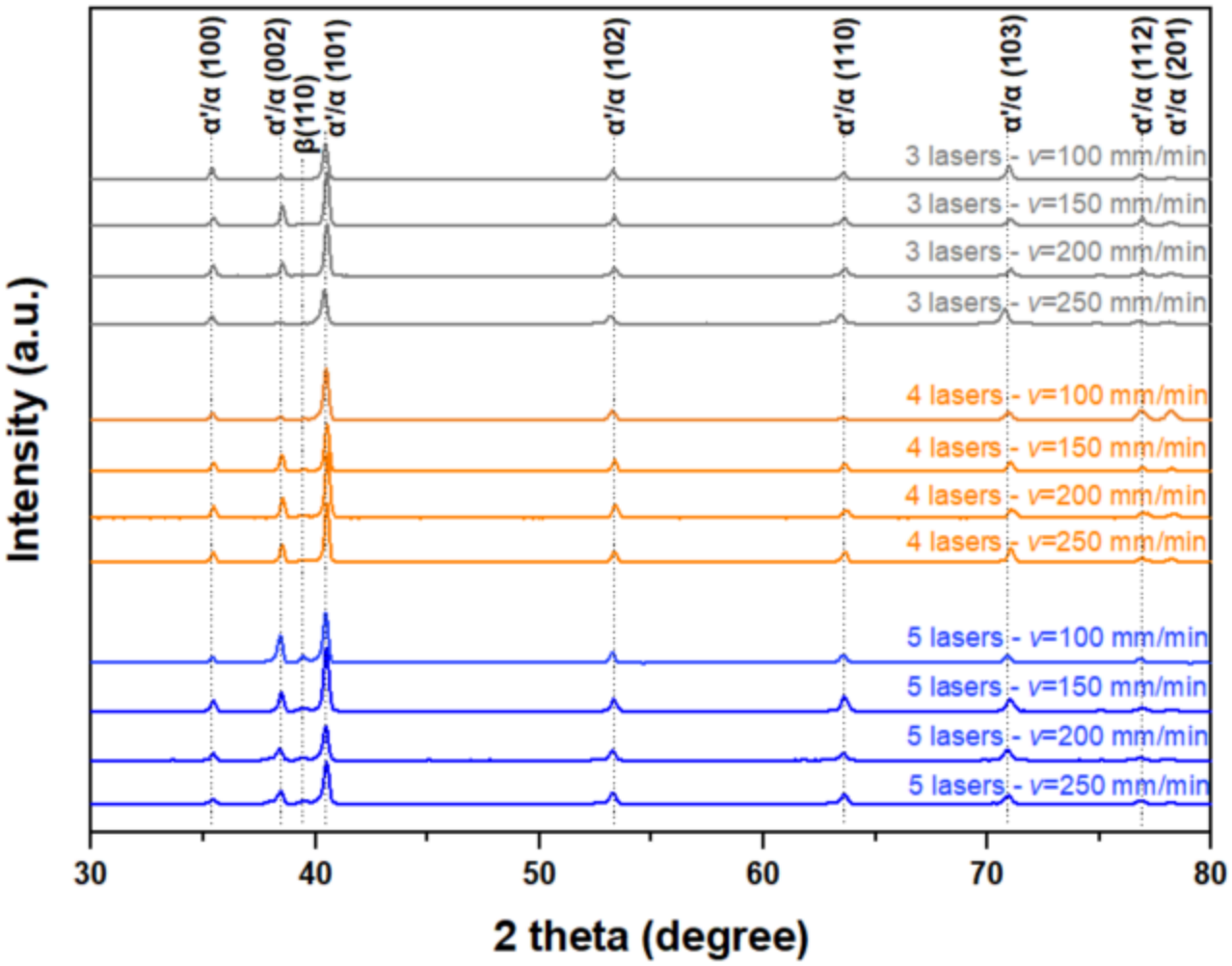


Figure 7

XRD phase identification for specimens fabricated with 3 lasers (gray data), 4 lasers (orange data), and 5 lasers (blue data) using varying scanning speeds.

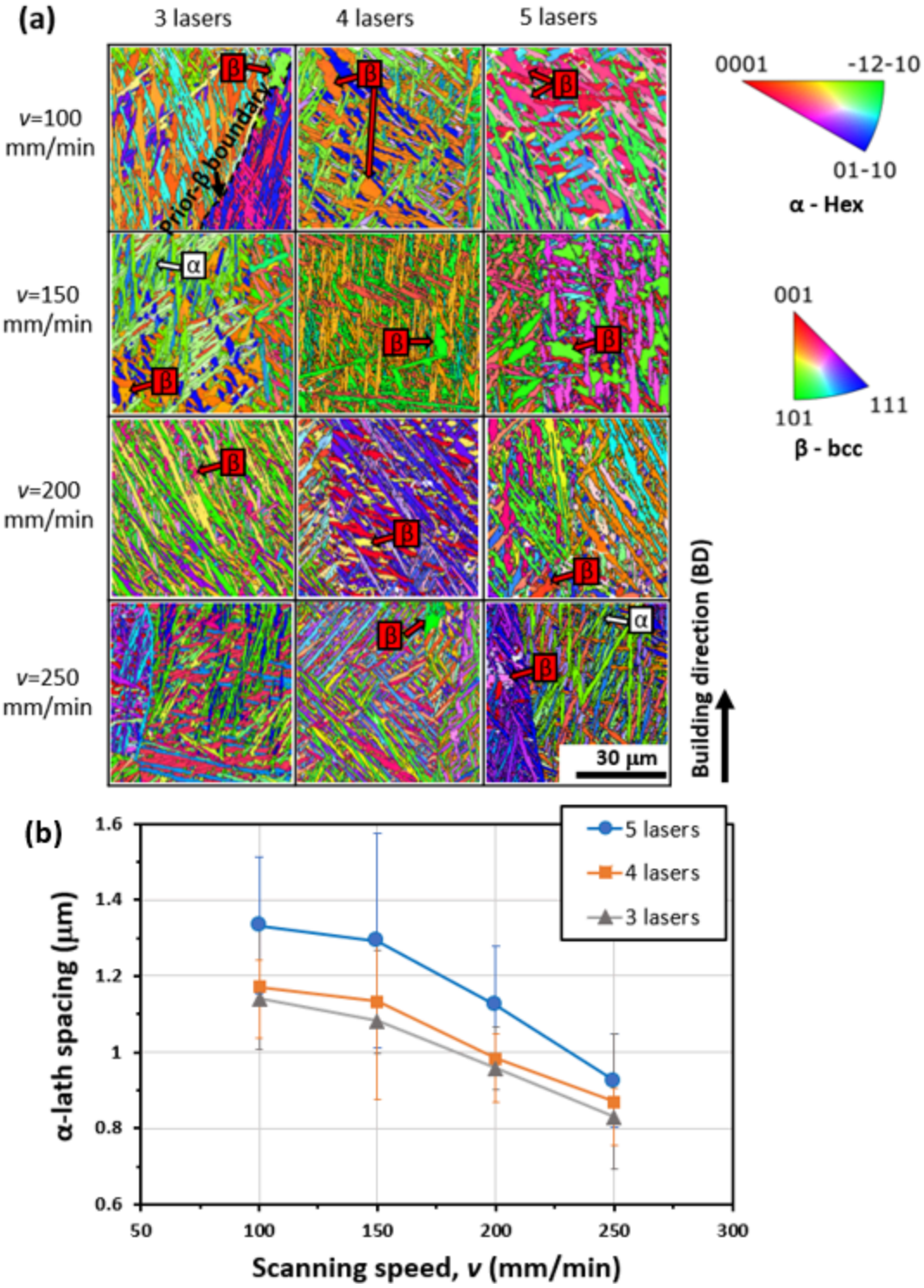


Figure 8

(a) EBSD orientation maps with respect to building direction (with a step size of 0.1 μm at 650 × magnification); (b) *α*-lath spacing for specimens fabricated with 3 lasers (gray data), 4 lasers (orange data), and 5 lasers (blue data) using varying scanning speeds.

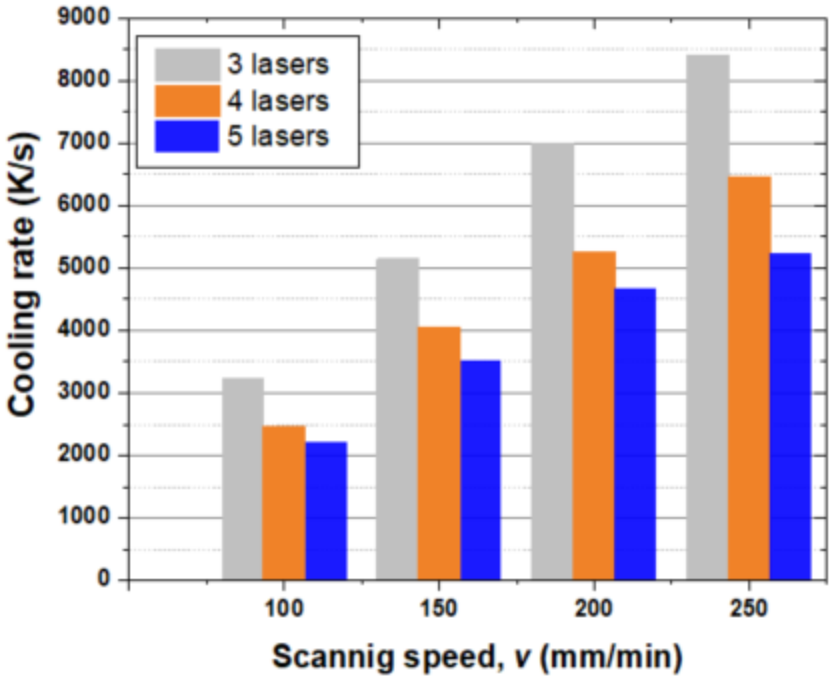


Figure 9

Predicted cooling rates for specimens fabricated with 3 lasers (gray data), 4 lasers (orange data), and 5 lasers (blue data) using varying scanning speeds.

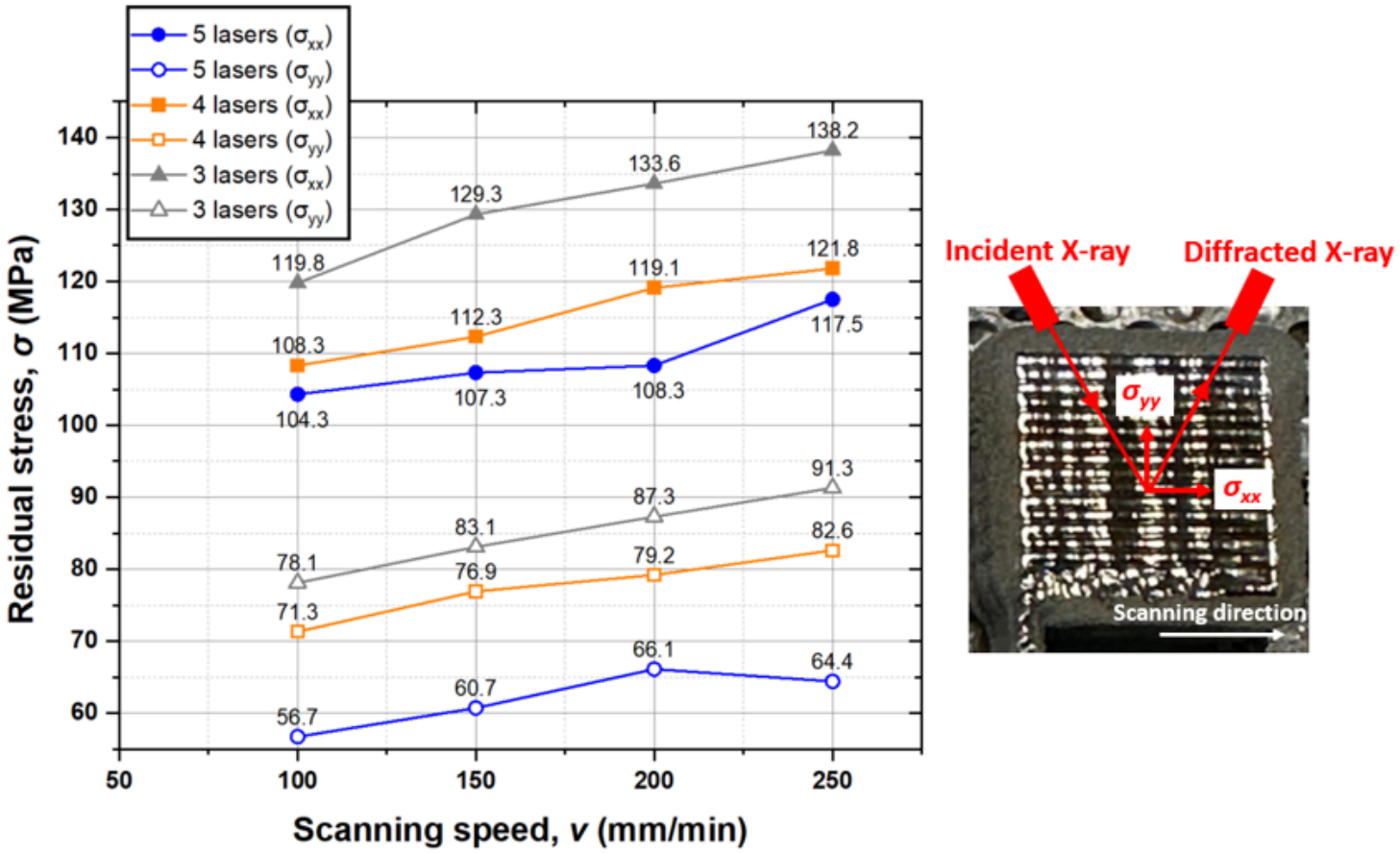


Figure 10

Residual stress in σ_{xx} direction (parallel to the scanning direction) and σ_{yy} direction (perpendicular to the scanning direction) for specimens fabricated with 3 lasers (gray data), 4 lasers (orange data), and 5 lasers (blue data) using varying scanning speeds.